Atmos. Chem. Phys. Discuss., https://doi.org/10.5194/acp-2017-1015
Manuscript under review for journal Atmos. Chem. Phys.
Discussion started: 22 November 2017

Atmospheric Chemistry and Physics Discussions

Size distribution and coating thickness of black carbon from the Canadian oil sands operations

Yuan Cheng[1], Shao-Meng Li[1,*], Mark Gordon[2], Peter Liu[1]

[1] Air Quality Research Division, Environment and Climate Change Canada, 4905 Dufferin Street, Toronto, Ontario M3H 5T4, Canada

[2] Department of Earth and Space Science and Engineering, York University, 4700 Keele Street, Toronto, Ontario M3J 1P3, Canada

* Corresponding author: shao-meng.li@canada.ca

Abstract

Black carbon (BC) plays an important role in the Earth's climate system. However, parameterization of BC size and mixing state have not been well addressed in aerosol-climate models, introducing substantial uncertainties into the estimation of radiative forcing by BC. In this study, we focused on BC emissions from the massive oil sands (OS) industry in northern Alberta, based on an aircraft campaign conducted over the Athabasca OS region in 2013. A total of 14 flights were made over the OS source area, in which the aircraft was typically flown in a 4- or 5-sided polygon pattern along flight tracks encircling an OS facility. Another 3 flights were performed downwind of the OS source area, each of which involved at least three intercepting locations where the well-mixed OS plume was measured along flight tracks perpendicular to the wind direction. Comparable size distributions were observed for refractory black carbon (rBC) over and downwind of the OS facilities, with rBC mass median diameters (MMD) between ~ 135 and 145 nm that were characteristic of fresh urban emissions. This MMD range corresponded to rBC number median diameters (NMD) of ~ 60−70 nm, approximately 100% higher than the NMD settings in some aerosol-climate models. The typical in- and out-of-plume segments of a flight, which had different rBC concentrations and photochemical ages, showed consistent rBC size distributions. Moreover, rBC size distributions remained unchanged at different downwind distances from the source area, suggesting that atmospheric aging would not necessarily change rBC size distribution. However, aging indeed influenced rBC mixing state. Coating thickness for rBC cores in the diameter range of 130−160 nm was nearly doubled within three hours when the OS plume was transported over a distance of 90 km from the source area.

Atmos. Chem. Phys. Discuss., https://doi.org/10.5194/acp-2017-1015
Manuscript under review for journal Atmos. Chem. Phys.
Discussion started: 22 November 2017

Atmospheric Chemistry and Physics Discussions

1. Introduction

Oil sands (OS), a type of unconventional petroleum deposit, are naturally occurring mixtures of bitumen (an extremely viscous form of crude oil), sand, water, and small amounts of other contaminants. The OS deposit in Alberta, Canada, is estimated to contain about 1.7 trillion barrels of bitumen. This deposit is distributed in the Athabasca, Cold Lake and Peace River regions, covering a total area of ~ 1.42×10^5 km^2, of which about 10% can be recovered economically with existing technologies (Government of Alberta, 2009). Bitumen can be recovered in two ways, i.e., surface mining for the shallow reserves (e.g., less than 75 m below the surface) and using in situ technologies for the deeper deposits. Surface mining can be applied to an area of only 4800 km^2 area within the Athabasca region; and by 2013, about 19% of this surface minable area had been disturbed (Alberta Energy, 2017). As demand for crude oil continues to increase, oil production from the Alberta oil sands has experienced rapid expansion over the last decade, with total OS production doubling between 2004 (1.1 million barrels per day, with about 66% from surface mining) and 2014 (2.2 million barrels per day, with about 47% from surface mining) (Alberta Energy, 2016).

The massive OS industry in Alberta has raised substantial concerns on environmental impacts. For example, studies by Kelly et al. (2009, 2010) and Kurek et al. (2013) showed that the OS development contributed substantial amounts of organic (e.g., polycyclic aromatic hydrocarbons, PAHs) and inorganic (e.g., mercury, nickel, and thallium) pollutants to the Athabasca River watershed. Moreover, model simulations by Parajulee and Wania (2014) indicated that the Canadian National Pollutant Release Inventory (NPRI) likely underestimated PAHs emissions in the Athabasca OS region. Despite these studies, both the emissions and subsequent environmental impacts remain poorly understood for pollutants from the Alberta OS industry. To address this lack of understanding, an aircraft campaign was conducted with measurements of an extensive set of air pollutants over the Athabasca OS region in the summer of 2013. Using results from the campaign, Shephard et al. (2015) validated profiles of ammonia, carbon monoxide, formic acid, and methanol retrieved from the Tropospheric Emission Spectrometer (TES) satellite; Liggio et al. (2016, 2017) demonstrated the large OS surface mining facilities in Athabasca as a significant source of secondary organic aerosol (SOA)

and gaseous organic acids; and Li et al. (2017) identified the surface mining facilities as a greater source of volatile organic compounds (VOCs) than previously realized.

In addition to gaseous pollutants and SOA, another focus of the 2013 aircraft campaign is black carbon (BC) emissions from the surface mining facilities and its transport downwind. BC is a distinct type of carbonaceous material formed during incomplete combustion of fossil and biomass fuels, which is strongly light-absorbing in the visible light spectral range, refractory, insoluble and typically appears as chain-like aggregates consisting of fewer than 10 to several hundred carbon spherules (Andreae and Gelencsér, 2006; Bond et al., 2013; Petzold et al., 2013; Buseck et al., 2014). BC plays a unique and important role in the Earth's climate system as an effective absorber of solar radiation. It has relatively short atmospheric residence times but can exert a strong warming effect on global and regional climate (Ramanathan and Carmichael, 2008; Bond et al., 2013; Myhre et al., 2013). Therefore, BC emission reduction has long been considered as an important near-term climate mitigation target. However, each step along the way between source and environmental effect of BC is complex. For example, anthropogenic BC emissions and the resulting temporal and spatial variations of BC, which can be simulated by chemical transport models, remain highly uncertain (Samset et al., 2014). On the other hand, parameterization of BC size and mixing state has not been well addressed in state-of-the-art radiative transfer models (Morgenstern et al., 2017). Both factors are recognized as important sources of uncertainties in the estimate of climate forcing by BC (IPCC, 2013).

For large-scale industrial activities such as the OS surface mining operations in Athabasca, key concerns regarding BC include (but are not limited to) the magnitude of BC emitted into the atmosphere, size distribution and mixing state of the freshly emitted BC particles, evolution of the BC particles including their size, mixing state and optical properties as the OS plumes are transported downwind, and BC deposition. In this study, a total of 17 flights conducted during the 2013 aircraft campaign were investigated to characterize BC emissions from six major OS surface mining facilities in the Athabasca region, with focuses on the evolution of BC size distribution and mixing state. Airborne BC measurements were performed by a Single Particle Soot Photometer (SP2). BC mass and number size distributions were determined and compared not only for different facilities but also for

Atmos. Chem. Phys. Discuss., https://doi.org/10.5194/acp-2017-1015
Manuscript under review for journal Atmos. Chem. Phys.
Discussion started: 22 November 2017

Atmospheric Chemistry and Physics Discussions

different downwind distances. It is commonly believed that BC cores in aged air masses are larger in size compared with those in fresh emissions (e.g., Moteki et al., 2007; McMeeking et al., 2010). Here we demonstrate that this is not necessarily the case. BC mixing state was estimated by coating thickness retrieved from the SP2, based on which the influences of photochemical aging were illustrated. Limitations of using this coating thickness to represent BC mixing state were also discussed. These results can provide insights into the evolution of BC aerosol in the real atmosphere.

2. Methods

2.1 Aircraft campaign

The aircraft campaign was conducted over the Athabasca OS region in northern Alberta between August 13 and September 7, 2013 in support of the Joint Canada-Alberta Implementation Plan for Oil Sands Monitoring (JOSM). Using a suite of state-of-the-art instruments installed aboard the National Research Council Institute for Aerospace Research Convair-580 research aircraft, an extensive set of air pollutants (including both gaseous and particulate species) were determined with high time resolutions (Gordon et al., 2015; Liggio et al., 2016; Li et al., 2017). During this campaign, 22 flights were made over the Athabasca OS region, for a total of about 84 hours. These flights were designed (1) to quantify emissions of air pollutants from six major OS surface mining facilities including Syncrude Mildred Lake (SML), Suncor Energy OSG (SUN), Canadian Natural Resources Limited Horizon (CNRL), Shell Albian and Jackpine (SAJ), Syncrude Aurora (SAU), and Imperial Kearl Lake (IKL), and (2) to determine atmospheric evolution of the primary pollutants. The details of the measurements, the flight patterns, and objectives of the flights were described in detail by Liggio et al. (2016) and Li et al. (2017). In 14 flights for emission quantitation, the aircraft was typically flown in a 4- or 5-sided polygon pattern encircling an OS surface mining facility, with level flight tracks at 8−10 altitudes increasing from 150 to 1370 m above ground; these level flight tracks were stacked along the sides of the polygon to form a virtual box encasing the facility (Figure 1a). Repeated emission flights were made over SML, SUN, CNRL, and SAJ, whereas single flights were made over SAU and IKL.

Three flights were designed to study transformation of air pollutants emitted from the OS surface mining facilities. They were conducted in a Lagrangian pattern such that the same OS plume was

Atmos. Chem. Phys. Discuss., https://doi.org/10.5194/acp-2017-1015
Manuscript under review for journal Atmos. Chem. Phys.
Discussion started: 22 November 2017

Atmospheric Chemistry and Physics Discussions

sampled at different time intervals (approximately 1 hour apart) as it was transported downwind from the source area (Figure 1b). Real-time wind speed and direction measurements were used to guide the intercepting locations. The first intercepting locations were chosen at about 1 hour downwind of the majority of the OS facilities so that the emitted air pollutants were well mixed and merged into large plumes. At each intercepting position, the aircraft was flown along level flight tracks perpendicular to the wind direction at multiple altitudes; then these level flight tracks were stacked vertically to create a virtual screen downwind of the OS source area. At least three screens were created for each transformation flight, without industrial emissions in between.

2.2 BC measurements by the SP2

A Single Particle Soot Photometer (SP2; Droplet Measurement Technologies Inc., Boulder, CO, USA) was used to measure the refractory black carbon (rBC) cores on a particle-by-particle basis based on incandescent light emitted from heated rBC cores when they cross and absorb energy from a laser beam (Stephens et al., 2003; Baumgardner et al., 2004; Schwarz et al., 2006; Moteki and Kondo, 2010; Laborde et al., 2012a). The SP2 used in this study detected single particle rBC cores in the mass range of ~ 0.3−16 fg, based on the calibration using regal black particles (Cappa et al., 2012). To account for the rBC cores outside this detection range, a lognormal fit was applied to the measured rBC size distribution and then extrapolated over 10−1000 nm (Schwarz et al., 2006). Here the rBC size refers to the mass equivalent diameter (D_{MEV}) calculated as $\left[\left(6\times m\right)/\left(\rho\times\pi\right)\right]^{1/3}$, where m and ρ are the mass and density of the rBC core, respectively. The value of ρ was assumed to be 1.8 g/cm^3, which corresponds to the median ρ value recommended by Bond and Bergstrom (2006). Using this ρ value, the rBC detection range could be converted to ~ 70−260 nm in terms of D_{MEV}. For either rBC mass or number concentration, a scaling factor (F_{rBC}) was calculated as $I_{whole}/I_{detected}$, where I_{whole} indicates the integral of the lognormal fitting curve from 10 nm to 1000 nm, and $I_{detected}$ indicates the integral of the curve from 70 nm to 260 nm. Subsequently, the final rBC concentration could be determined as $F_{rBC} \times C_{detected}$, where $C_{detected}$ is the detected rBC concentration (either mass or number) measured by the SP2. All the rBC concentrations involved in this paper have been scaled by F_{rBC}.

Atmos. Chem. Phys. Discuss., https://doi.org/10.5194/acp-2017-1015
Manuscript under review for journal Atmos. Chem. Phys.
Discussion started: 22 November 2017

Atmospheric Chemistry and Physics Discussions

In addition to emitting incandescent radiation, rBC containing particles also scatter light when passing through the laser beam of the SP2. Coating thicknesses on rBC cores ($T_{coating}$, in nm) can be retrieved from the scattering signals on a particle-by-particle basis, using Mie theory calculation with a series of assumptions (Schwarz et al., 2008a, b; Laborde et al., 2012b). To calculate $T_{coating}$ for an rBC containing particle, the internally mixed particle needs to be idealized as a two-component sphere with a concentric core-shell morphology. In this study, the rBC core was assumed to have a complex refractive index of 2.26 – 1.26*i*, which was initially suggested by Moteki et al. (2010) and subsequently confirmed by Taylor et al. (2015). The coating material on a rBC core was assumed to have a complex refractive index of 1.5 – 0*i*, which is representative of the corresponding values determined for inorganic salts (e.g., ammonium sulfate) and secondary organic aerosol (Schnaiter et al., 2005; Lambe et al., 2013). The core size was held fixed at D_{MEV} of the rBC core, whereas the diameter of the whole particle was varied in the Mie calculation until the modeled scattering cross section matched the measurement. Measured scattering cross section was determined by a leading-edge-only (LEO) fit to the recorded scattering signal (Gao et al., 2007). Finally, $T_{coating}$ was calculated as the difference between the radii of the whole particle and the rBC core.

3. Results and Discussion

3.1 rBC size distributions over the OS source region: facility-integrated results

For each flight, the measured masses of the individual rBC cores over the entire flight were first grouped into different size bins and then fitted by a lognormal curve:

$$\frac{\mathrm{d}m}{\mathrm{d}\log D_{MEV}} = A_{mass} \times \exp\left\{0 - \left[\frac{\ln\left(D_{MEV}/X_{1,\,mass}\right)}{X_{2,\,mass}}\right]^2\right\} \quad (1)$$

where A_{mass}, $X_{1,\,mass}$ and $X_{2,\,mass}$ are the fitting parameters. The fitting parameter $X_{1,\,mass}$ will be termed the mass median diameter (MMD), and the fitting parameter $X_{2,\,mass}$ will be loosely referred to as the mass distribution width. As can be seen from Equation (1), A_{mass} is proportional to the absolute value of rBC mass concentration and thus it is unimportant for describing the shape of a lognormal curve. This is particularly the case for comparison of rBC size distributions among different OS facilities. It

Atmos. Chem. Phys. Discuss., https://doi.org/10.5194/acp-2017-1015
Manuscript under review for journal Atmos. Chem. Phys.
Discussion started: 22 November 2017

Atmospheric Chemistry and Physics Discussions

should also be noted that the mass-based scaling factor ($F_{\mathrm{rBC,\ mass}}$), which accounts for the rBC masses outside the SP2's detection range, is independent of A_{mass}. Therefore, A_{mass} will not be further discussed in rBC size distribution. Similarly, rBC number-size distribution could be expressed as:

$$\frac{\mathrm{d}N}{\mathrm{d}\log D_{\mathrm{MEV}}} = A_{\mathrm{number}} \times \exp\left\{0 - \left[\frac{\ln\left(D_{\mathrm{MEV}}/X_{1,\ \mathrm{number}}\right)}{X_{2,\ \mathrm{number}}}\right]^2\right\} \quad (2)$$

where A_{number}, $X_{1,\ \mathrm{number}}$ and $X_{2,\ \mathrm{number}}$ are the fitting parameters. $X_{1,\ \mathrm{number}}$ and $X_{2,\ \mathrm{number}}$ will be termed the number median diameter (NMD) and the number distribution width, respectively.

Mass and number size distributions of rBC are summarized in Figure 2 for the 14 emission flights. As shown in Figure 2, the rBC MMD and NMD were typically in the range of 135−145 nm and 60−70 nm, respectively, while both the mass and number distribution widths were approximately 0.7. Most of the rBC from the surface mining facilities were from the heavy diesel trucks used to transport the mined oil sands ores to centralized locations in each facility for bitumen separation from the sands. In most cases, rBC emissions from the six major OS surface mining facilities exhibited similar size distributions. These rBC size distributions are comparable with those observed for urban emissions and source (or near-source) samples representing different types of engine exhausts. For example, (1) during an airborne measurement conducted as part of the CalNex 2010 campaign, rBC MMD was estimated to be 122 nm over the Los Angeles Basin (Metcalf, et al., 2012); (2) rBC MMD observed in the urban outflows were typically in the range of 140−180 nm, as evidenced by ground-based measurement downwind of Tokyo (Shiraiwa et al., 2007), and by aircraft-based observations over Texas (Schwarz et al., 2008a), California (Sahu et al., 2012) and western and northern Europe (McMeeking et al., 2010); (3) when mainly impacted by traffic emissions, rBC MMD were about 100 and 120 nm for a suburban site in Paris (Laborde et al., 2013) and an urban site in London (Liu et al., 2014), respectively; (4) rBC MMD measured at urban sites in Tokyo, Japan (Kondo et al., 2011b) and Sacramento, CA (Cappa et al., 2012) were between 140 and 150 nm; (5) a laboratory study showed that the MMD was about 125 nm for rBC cores emitted from a diesel car (Laborde et al., 2012b); (6) a MMD of 126 nm was observed for rBC at the Cranfield airport in UK, attributable to aircraft engine

exhausts (McMeeking et al., 2010). Although not all of these studies determined rBC MMD and NMD simultaneously, rBC NMD were typically in the range of ~ 60 to 70 nm for urban emissions dominated by contributions from fossil fuel combustion (e.g., Schwarz et al., 2008a; Kondo et al., 2011b; Metcalf, et al., 2012).

A comparison of rBC size distributions between this study and previous ones also suggests that rBC cores emitted from fossil fuel combustion were smaller in size compared to those from biomass burning. The rBC MMD and NMD measured in biomass burning plumes were typically around 200 and 140 nm, respectively, which were supported by airborne measurements over Texas (Schwarz et al., 2008a), California (Sahu et al., 2012), Canada (Kondo et al., 2011a; Taylor et al., 2014) and the Arctic (Kondo et al., 2011a). However, wet deposition could lead to a large decrease (e.g., as much as 50 nm) in the MMD of rBC cores in biomass burning plumes (Taylor et al., 2014), suggesting that an rBC MMD substantially smaller than 200 nm does not exclude the possibility of biomass burning emission contributions.

Different assumptions have been made by aerosol-climate models for the size distribution of black carbon. For example, the NMD of black carbon emitted by fossil fuel combustion were assumed to be 30, 40 and 60 nm by Dentener et al. (2006; for AeroCom Phase I models), Heald et al. (2014; for a radiative transfer model coupled with GEOS-Chem) and Stier et al. (2005; for the aerosol-climate modelling system ECHAM5-HAM), respectively. According to the SP2 measurement results on rBC, including those from the present study, a NMD of 60 nm would be a more appropriate input parameter in the models for black carbon emissions from fossil fuel combustion.

3.2 rBC size distributions over the OS source region: time-resolved results

In addition to the facility-integrated results (Figure 2), log-normal fits were also applied to 2-min intervals of rBC data derived from the SP2. Figure 3 and 4 show results from the emission flights conducted for CNRL on August 26, 2013 (i.e., F_8/26) and for SUN on August 28, 2013 (i.e., F_8/28), respectively. In both cases, the rBC mass and number size distributions did not exhibit major temporal variations, despite the minor fluctuations observed during F_8/28. The stable rBC size distribution within a flight can be more readily seen from Figure 5a, which indicates that the rBC MMD, mass

Atmos. Chem. Phys. Discuss., https://doi.org/10.5194/acp-2017-1015
Manuscript under review for journal Atmos. Chem. Phys.
Discussion started: 22 November 2017

Atmospheric Chemistry and Physics Discussions

distribution width and therefore the mass-based scaling factor ($F_{rBC,\ mass}$) were independent of rBC concentration. As shown in Figure 5a and Table 1, the variations of rBC MMD, mass distribution width, and $F_{rBC,\ mass}$ were within 5% for F_8/26. Larger variations in rBC size distribution were observed for F_8/28, but the variations in these three parameters were still within 10%. The variations of rBC NMD, number distribution width, and number-based scaling factor ($F_{rBC,\ number}$) were also within 10% for both F_8/26 and F_8/28 (Table 1).

The temporal variations of rBC concentration shown in Figure 3 and 4 were mainly driven by the in- vs. out-of-plume differences. There were a sharp increase in rBC concentration when the aircraft flew into a plume, whereas the rBC concentration deceased rapidly when the aircraft left the plume. Therefore, the stable rBC size distributions observed for the emission flights, which were clearly independent of rBC concentration (e.g., Figure 5a), mean negligible in- vs. out-of-plume differences in rBC size distributions over the OS source region. The size distribution consistency for rBC is observed regardless of the threshold rBC concentration used to distinguish the in- and out-of-plume conditions, which is flight-dependent (e.g., ~ 0.1 μg/m^3 in terms of 2-min averaged rBC mass concentration for F_8/26 as shown in Figure S1). The implications of consistent size distributions for rBC near the sources are further discussed in Section 3.3 together with results from the transformation flights.

In addition to rBC concentration, the in- and out-of-plume air masses had different photochemical ages. Here a photochemical age is calculated as $-\log_{10}(NO_x/NO_y)$, where NO_x is the sum of nitrogen monoxide and nitrogen dioxide (i.e., NO + NO_2) and NO_y refers to the total reactive oxidized nitrogen compounds (Kleinman et al., 2008). Measurement of NO_x and NO_y during the aircraft campaign has been described elsewhere (Liggio et al., 2016). As shown in Figure 5b, there was a robust negative correlation between the rBC mass concentration and photochemical age, which likely reflects the connection between air mass dilution and aging. Compared to the in-plume segments of a flight, the out-of-plume ones were characterized by not only lower rBC concentrations but also older photochemical ages. Given the clear dependence of rBC concentration on photochemical age (Figure 5b) and the stable rBC size distribution across the whole rBC

Atmos. Chem. Phys. Discuss., https://doi.org/10.5194/acp-2017-1015
Manuscript under review for journal Atmos. Chem. Phys.
Discussion started: 22 November 2017

Atmospheric Chemistry and Physics Discussions

concentration range observed within an emission flight (Figure 5a and Table 1), it could be inferred that rBC size distribution was independent of photochemical age over the OS source region.

3.3 rBC size distributions downwind of the OS source region

Mass and number size distributions of rBC are shown in Figure 6 and 7, respectively, for the transformation flight conducted on September 4, 2013 (i.e., F_9/4) which reached a downwind distance of approximately 120 km (relative to the downwind edge of the OS source area; Figure 1b). As can be seen from the time-resolved log-normal fitting results (Figure 6a and 7a), both the rBC mass and number size distributions were fairly stable during F_9/4, without major temporal change patterns. For the typical in- and out-of-plume conditions of F_9/4, the rBC MMD were 143.39 ± 0.95 and 141.56 ± 1.19 nm with mass distribution widths of 0.72 ± 0.01 and 0.71 ± 0.02, respectively (Figure 6b); the rBC NMD were 70.65 ± 0.42 and 69.02 ± 0.46 nm with number distribution widths of 0.68 ± 0.01 and 0.69 ± 0.01, respectively (Figure 7b). These rBC size distributions (Figure 6b and 7b) were derived from the SP2 measurements performed on the various virtual screens, where the aircraft was flown along level flight tracks (primarily at ~ 450 and 600 m) perpendicular to the wind direction. For the level flight tracks, the typical in- and out-of-plume conditions (i.e., segments) were distinguished by rBC concentration (Figure 8), i.e., the typical out-of-plume conditions were identified by relatively low and constant rBC concentrations whereas the typical in-plume conditions were characterized by sharp increases in rBC concentration above the out-of-plume level. In Figure 6b, the rBC mass size distribution was scaled for the out-of-plume conditions to reveal their lower rBC concentrations compared to the in-plume conditions (Figure 6d). When performing the scaling, the in-plume rBC size distribution was used as a reference (i.e., kept unchanged). The out-of-plume rBC size distribution was scaled to make the $I_{\text{out-of-plume, scaled}}$ to $I_{\text{in-plume}}$ ratio equal the $\text{rBC}_{\text{out-of-plume}}$ to $\text{rBC}_{\text{in-plume}}$ ratio, where the individual terms, in sequence, represent integral of the scaled out-of-plume rBC size distribution curve, integral of the reference in-plume rBC size distribution curve, the average out-of-plume rBC mass concentration (54.22 ng/m^3, derived from Figure 6d), and the average in-plume rBC concentration (207.93 ng/m^3, derived from Figure 6d). In Figure 7b, the out-of-plume rBC number

size distribution was scaled in the same way. As can be seen from Figure 6b and 7b, the in- vs. out-of-plume difference was negligible for rBC size distribution downwind of the OS region.

Photochemical ages were older for the out-of-plume conditions compared to the in-plume ones, by ~ 0.3−0.5 in terms of $-\log_{10}(NO_x/NO_y)$ for different screens of F_9/4 (Figure 6e). Therefore, the consistent rBC size distributions between the in- and out-of-plume conditions indicated that photochemical age had little influence on rBC size distribution downwind of the OS region. This conclusion was also strongly supported by the comparison of in-plume rBC size distributions among different downwind distances. As the OS plume was transported downwind, the in-plume rBC concentration decreased due to dilution (Figure 6d), from ~ 310 ng/m^3 for the first screen (screen #1) to ~ 110 ng/m^3 for the fourth screen (screen #4); on the other hand, the in-plume photochemical age $-\log_{10}(NO_x/NO_y)$ increased (Figure 6e), from ~ 0.1 for screen #1 to ~ 0.5 for screen #4. The last screen (screen #5) did not differ largely from screen #4 with respect to either in-plume rBC concentration or photochemical age, appearing to indicate that the dilution and aging processes had slowed down or even stopped since screen #4. However, it should be noted that unlike the first four screens, screen #5 did not captured the full OS plume, i.e., the plume edges were missed. Compared to the central portion of the plume, the plume edges had lower rBC concentrations and older photochemical ages. Therefore, the average rBC concentration and $-\log_{10}(NO_x/NO_y)$ could not be compared directly between screen #5 and the first four screens, and consequently, results from screen #5 were not involved in Figure 6d and 6e. Nonetheless, for all successive screens of F_9/4, the in-plume rBC MMD and NMD were found to fall into a narrow range of 140−145 and 69−72 nm, respectively, while both the mass and number distribution widths were about 0.7 (Figure 6c, 7c and 9). In Figure 6c and 7c, rBC size distributions derived from successive screens were scaled to show the decreases in rBC concentration caused by dilution, using the same approach as that described in detail for Figure 6b. The scaling requires rBC concentration representative of the full plume and thus was not performed for screen #5. A direct comparison of rBC size distributions between screen #5 and the first four screens is provided by Figure 9. Figure 9 also demonstrates consistent in-plume rBC size distributions among successive screens for the other two transformation flights that were conducted on

Atmos. Chem. Phys. Discuss., https://doi.org/10.5194/acp-2017-1015
Manuscript under review for journal Atmos. Chem. Phys.
Discussion started: 22 November 2017

August 19 and September 5, 2013, respectively (i.e., F_8/19 and F_9/5), providing further solid evidence for the negligible influence of atmospheric aging on rBC size distribution downwind of the OS source region.

Previous studies conducted in remote areas (either ground- or aircraft-based) typically showed rBC MMD between 200 and 220 nm (Shiraiwa et al., 2008; Liu et al., 2010; McMeeking et al., 2010; Schwarz et al., 2010), substantially higher than those observed over urban areas (e.g., 122 nm over the Los Angeles basin; Metcalf et al., 2012) or at urban locations (e.g., 146 nm in Tokyo, Japan; Kondo et al., 2011b). Therefore, it has been commonly believed that rBC cores in aged air masses are larger than those in fresh emissions. However, results from the present study indicate that this is not necessarily the case. It is inferred that not all aging processes will change rBC size distribution and instead, influences of aging on rBC size distribution depend on the presence of atmospheric processes that can lead to increased rBC core mass and size in a single particle (e.g., evaporation of cloud droplets containing multiple rBC particles). In this study, it appears that no such processes were at play, and within the photochemical ages encountered, rBC core masses and sizes did not change.

In addition to the evolution of in-plume rBC concentration, Figure 6d shows that the out-of-plume rBC concentration decreased until screen #3. This decrease was associated with an increase in $-\log_{10}(NO_x/NO_y)$ for the out-of-plume conditions (Figure 6e). For screen #4, both the out-of-plume rBC concentration and photochemical age were nearly the same as the respective values observed for screen #3. Therefore, the out-of-plume conditions identified for screens #3 and #4 should be more representative of the background. For screens #3 and #4, rBC size distributions agreed well between the in- and out-of-plume conditions, within ± 3 nm in terms of MMD or NMD, indicating that the background did not differ significantly from the OS emissions with respect to rBC size distribution. Consistent in- and out-of-plume rBC size distributions observed at smaller downwind distances (i.e., for screens #1 and #2) and over the OS source area (i.e., for the emission flights) pointed to the same conclusion, although the out-of-plume conditions in these cases were less representative of the background. rBC cores in the background could be from the OS emissions and/or long-range transported urban emissions that had not been influenced by atmospheric processes that can change

Atmos. Chem. Phys. Discuss., https://doi.org/10.5194/acp-2017-1015
Manuscript under review for journal Atmos. Chem. Phys.
Discussion started: 22 November 2017

single particle rBC core size. These two kinds of emissions did not differ largely in rBC size distribution (as discussed in section 3.1) and therefore they were difficult to be further distinguished only by rBC size.

3.4 Evolution of rBC mixing state

A key step to retrieve coating thickness ($T_{coating}$) of an rBC containing particle from its scattering signal is the LEO fit, which requires, at least, the leading edge of the scattering signal ($S_{leading\text{-}edge}$) can be properly measured (Schwarz et al., 2008a, b; Laborde et al., 2012b; Liu et al., 2014). However, the LEO fit cannot be performed when $S_{leading\text{-}edge}$ is outside the SP2's detection range of scattering intensity; thus, $T_{coating}$ cannot be calculated for relatively small rBC cores with thin coatings (i.e., rBC containing particles with $S_{leading\text{-}edge}$ below the lower detection limit of scattering intensity) or relatively large rBC cores with thick coatings (i.e., rBC containing particles with $S_{leading\text{-}edge}$ above the upper detection limit of scattering intensity) (Metcalf et al., 2012; Dahlkötter et al., 2014). This limitation prohibits a direct comparison of $T_{coating}$ across all rBC cores with different sizes. In this study, $T_{coating}$ was found to exhibit a decreasing trend with the increase in rBC D_{MEV} for both the transformation (Figure 10) and emission flights (Figure S2). This trend was primarily attributed to the limitation that the detection range of $T_{coating}$ is rBC D_{MEV} dependent, rather than indicating that relatively small rBC cores were more thickly coated than larger cores.

Besides $T_{coating}$, the fraction of rBC cores that can be assigned a coating thickness ($F_{assigned}$, in %) was also rBC D_{MEV} dependent such that $F_{assigned}$ was found to be the highest (between ~ 35−45%) for rBC cores in the D_{MEV} range of 130−160 nm (Figure 10 and S2). The rBC containing particles in this D_{MEV} range were selected for further discussions on $T_{coating}$ (their $T_{coating}$ will be specified as T*), with a focus on the evolution of rBC mixing state as the OS plumes were transported downwind. As shown in Figure 11a for the transformation flight F_9/4, the in-plume T* exhibited an increasing trend with the increase in downwind distance or transport time, e.g., from ~ 22 nm for screen #1 to ~ 41 nm for screen #4. This trend is not surprising given the continuous formation of SOA during transport of the OS plumes (Liggio et al., 2016). For rBC near the sources, T* was close to zero as observed from the emission flights over the OS facilities. For example, T* was derived at ~ 3 nm for F_9/3 (Figure S2).

Atmos. Chem. Phys. Discuss., https://doi.org/10.5194/acp-2017-1015
Manuscript under review for journal Atmos. Chem. Phys.
Discussion started: 22 November 2017

Atmospheric Chemistry and Physics Discussions

These freshly emitted rBC cores grew a coating of ~ 20 nm thickness in the first hour after emission, when the OS plume was transported from the sources in the OS facilities to the downwind edge of the OS region.

*T** were found to be comparable between the in- and out-of-plume conditions for screen #1, which were ~ 22 and 23 nm, respectively (Figure 11a). It is unlikely that the out-of-plume *T** could be as low was ~ 23 nm, if the majority of the out-of-plume rBC cores were from long-range transport and thus had an aging time of much longer than one hour. Therefore, the rBC cores observed in the out-of-plume conditions should also be influenced by emissions in the oil sands region albeit at much lower air concentrations compared to the plumes, such as from on road traffic that was not part of any oil sands surface mining facility.

Compared to the in-plume conditions, the increase in *T** was smaller for the out-of-plume conditions as the OS plume was further transported from screen #1 (Figure 11a) and moreover, the out-of-plume *T** stopped increasing after screen #3 such that it was ~ 32 nm for both screens #3 and #4. One explanation for the different evolution patterns of the in- and out-of-plume *T**, which had comparable initial values (i.e., those for screen #1), is the less effective formation of coating materials (e.g., SOA and sulfate) for the out-of-plume conditions than in plumes, given that coating precursors (volatile organic compounds and sulfur dioxide) were much more abundant in the plumes from which fast formation of organic aerosols was observed (Liggio et al., 2016). As shown in Figure 11b, the in-plume OA to rBC ratio exhibited a robust increasing trend with the increase in downwind distance (e.g., by ~ 150% for screen #4 relative to screen #1), whereas the increase in OA to rBC ratio was less significant for the out-of-plume condition (e.g., by only ~ 45% for screen #4 compared to screen #1) which was negligible between screens #3 and #4.

We did not compare $T_{coating}$ measured in this study with results from previous ones due to the following reasons. (1) The detection range of $T_{coating}$ and therefore the estimated $T_{coating}$ depend on the SP2's detection range of scattering intensity, which could differ substantially among different SP2 instruments. This dependency indicates that different SP2 instruments might lead to different $T_{coating}$ estimates even for the same ensemble of rBC containing particles. (2) The detection range of $T_{coating}$

Atmos. Chem. Phys. Discuss., https://doi.org/10.5194/acp-2017-1015
Manuscript under review for journal Atmos. Chem. Phys.
Discussion started: 22 November 2017

and therefore the estimated $T_{coating}$ also depend on the rBC core size (i.e., D_{MEV}). Quite different D_{MEV} ranges have been used by previous studies to estimate $T_{coating}$, e.g., 190−210 nm by Schwarz et al. (2008a, b) vs. 162−185 nm by Langridge et al. (2012), indicating that these $T_{coating}$ estimates are not directly comparable. (3) The $T_{coating}$ estimates could be considerably influenced by uncertainties introduced by the LEO fit. These uncertainties can be evaluated using non-rBC containing particles. The scattering signals of non-rBC containing particles always have the shape of a full Gaussian curve, since they will not evaporate or change in size when passing through the SP2's laser beam. Thus, for non-rBC containing particles, the LEO fit should in principle lead to the same scattering amplitude or the same optical size ($D_{optical}$) as that retrieved from a fit to the full scattering signal (i.e., the full-Gaussian fit) (Gao et al., 2007). In this study (Figure 12), the LEO and full-Gaussian fits agreed within approximately ± 15% in terms of $D_{optical}$ for non-rBC containing particles. Here the $D_{optical}$ was calculated from the fitted scattering amplitudes, by assuming a complex refractive index of 1.5 – 0i for non-rBC containing particles. $D_{optical}$ was used in Figure 12 to evaluate the agreement between the LEO and full-Gaussian fits because it was more directly related to $T_{coating}$ compared to the scattering amplitude. However, comparison of the LEO and full-Gaussian fits for the determination of $D_{optical}$ or scattering amplitude was not presented in many previous publications involving $T_{coating}$. This is a substantial concern because the LEO fit has been considered reliable as long as the LEO to full-Gaussian ratios are relatively constant (not necessarily around 1.0) for the fitted scattering amplitudes (e.g., Metcalf, et al., 2010). Since an agreement between the LEO and full-Gaussian fits was not always required, previously reported $T_{coating}$ might be biased by the LEO-induced uncertainty to different extents, adding to the difficulties in comparing $T_{coating}$ across studies.

4. Conclusions

An aircraft campaign was conducted over the Athabasca oil sands region in the summer of 2013, during which the size distribution and coating thickness of refractive black carbon (rBC) cores were studied as they were emitted from the sources and as they were transported downwind. The rBC size distributions were found to be comparable at the six major OS surface mining facilities, typically with mass median diameters (MMD) of 135–145 nm and number median diameters (NMD) of 60–70 nm

that were characteristic of fresh urban emissions dominated by contributions from fossil fuel combustion. The results from the present study indicate that the size distributions assumed in some aerosol-climate models for fossil fuel BC have NMD (e.g., 30 nm) which are likely too low by a factor of 2 compared to the present results as well as previously reported values. An NMD of 60 nm would be more appropriate for fossil fuel BC. The observed rBC size distributions were consistent not only for the typical in- and out-of-plume segments of a flight (either emission or transformation) but also for different downwind distances form the OS source area, indicating little dependence of the rBC size distribution on atmospheric aging within 4 to 5 hours from the point of emission.

The coating thicknesses ($T_{coating}$) were retrieved for rBC containing particles from their scattering signals, on a particle-by-particle basis. Mainly due to the SP2's limited detection range of scattering intensity, $T_{coating}$ could not be calculated for all the detected rBC cores. The fraction of rBC cores that can be assigned a coating thickness was found to be the highest but still lower than 50% for those in the diameter range of 130−160 nm. It is not surprising that $T_{coating}$ increased as the OS plumes were transported downwind, resulting from the formation mainly of secondary organic aerosols but also of sulfate. Such coating increase with aging can significantly change the optical properties of the rBC containing particles and hence their potentials for radiative forcing. Based on the present $T_{coating}$ results, however, estimates of these effects are challenging, mainly because $T_{coating}$ was unknown for the majority of the rBC containing particles.

Acknowledgements

We would like to thank the National Research Council of Canada flight crew of the Convair-580, the technical support staff of the Air Quality Research Division, and Dr. Stewart Cober for the management of the study. This project was supported by Environment and Climate Change Canada's Climate and Clean Air Programme (CCAP) and the Canada-Alberta Joint Oil Sands Monitoring program.

References

Alberta Energy: Oil Sands Production Profile: 2004-2014, ISBN: 978-1-4601-2723-0, 2016.

426 Alberta Energy: Oil Sands Facts and Statistics, available at
427 http://www.energy.alberta.ca/OilSands/791.asp, last accessed on March 28, 2017.
428 Andreae, M. O. and Gelencsér, A.: Black carbon or brown carbon? The nature of light-absorbing
429 carbonaceous aerosols, Atmos. Chem. Phys., 6, 3131–3148, 2006.
430 Baumgardner, D., Kok, G., and Raga, G.: Warming of the Arctic lower stratosphere by light absorbing
431 particles, Geophys. Res. Lett., 31, L06117, doi:10.1029/2003GL018883, 2004.
432 Bond, T. C. and Bergstrom, R. W.: Light absorption by carbonaceous particles: an investigative
433 review, Aerosol Sci. Technol., 40, 27–67, 2006.
434 Bond, T. C., Doherty, S. J., Fahey, D. W., Forster, P. M., Berntsen, T., DeAngelo, B. J., Flanner, M.
435 G., Ghan, S., Kärcher, B., Koch, D., Kinne, S., Kondo, Y., Quinn, P. K., Sarofim, M. C., Schultz,
436 M. G., Schulz, M., Venkataraman, C., Zhang, H., Zhang, S., Bellouin, N., Guttikunda, S. K.,
437 Hopke, P. K., Jacobson, M. Z., Kaiser, J. W., Klimont, Z., Lohmann, U., Schwarz, J. P., Shindell,
438 D., Storelvmo, T., Warren, S. G., and Zender, C. S.: Bounding the role of black carbon in the
439 climate system: a scientific assessment, J. Geophys. Res., 118, 5380–5552,
440 doi:10.1002/jgrd.50171, 2013.
441 Buseck, P. R., Adachi, K., Gelencsér, A., Tompa, É., and Pósfai, M.: Ns-Soot: a material-based term
442 for strongly light-absorbing carbonaceous particles, Aerosol Sci. Technol., 48, 777–788, 2014.
443 Cappa, C. D., Onasch, T. B., Massoli, P., Worsnop, D. R., Bates, T. S., Cross, E. S., Davidovits, P.,
444 Hakala, J., Hayden, K. L., Jobson, B. T., Kolesar, K. R., Lack, D. A., Lerner, B. M., Li, S. M.,
445 Mellon, D., Nuaaman, I., Olfert, J. S., Petäjä, T., Quinn, P. K., Song, C., Subramanian, R.,
446 Williams, E. J., and Zaveri, R. A.: Radiative absorption enhancements due to the mixing state of
447 atmospheric black carbon, Science, 337, 1078–1081, 2012.
448 Dahlkötter, F., Gysel, M., Sauer, D., Minikin, A., Baumann, R., Seifert, P., Ansmann, A., Fromm, M.,
449 Voigt, C., and Weinzierl, B.: The Pagami Creek smoke plume after long-range transport to the
450 upper troposphere over Europe – aerosol properties and black carbon mixing state, Atmos. Chem.
451 Phys., 14, 6111–6137, 2014.

452 Dentener, F., Kinne, S., Bond, T., Boucher, O., Cofala, J., Generoso, S., Ginoux, P., Gong, S.,
453 Hoelzemann, J. J., Ito, A., Marelli, L., Penner, J. E., Putaud, J. P., Textor, C., Schulz, M., van der
454 Werf, G. R., and Wilson, J.: Emissions of primary aerosol and precursor gases in the years 2000
455 and 1750 prescribed data-sets for AeroCom, Atmos. Chem. Phys., 6, 4321–4344, 2006.
456 Gao, R. S., Schwarz, J. P., Kelly, K. K., Fahey, D. W., Watts, L. A., Thompson, T. L., Spackman, J.
457 R., Slowik, J. G., Cross, E. S., Han, J. H., Davidovits, P., Onasch, T. B., and Worsnop, D. R.: A
458 novel method for estimating light-scattering properties of soot aerosols using a modified Single-
459 Particle Soot Photometer, Aerosol Sci. Technol., 41, 125–135, 2007.
460 Gordon, M., Li, S. M., Staebler, R., Darlington, A., Hayden, K., O'Brien, J., and Wolde, M.:
461 Determining air pollutant emission rates based on mass balance using airborne measurement data
462 over the Alberta oil sands operations. Atmos. Meas. Tech., 8, 3745–3765, 2015.
463 Government of Alberta: Environmental Management of Alberta's Oil Sands, ISBN: 978-0-7785-7677-
464 8, 2009.
465 Heald, C. L., Ridley, D. A., Kroll, J. H., Barrett, S. R. H., Cady-Pereira, K. E., Alvarado, M. J., and
466 Holmes, C. D., Contrasting the direct radiative effect and direct radiative forcing of aerosols,
467 Atmos. Chem. Phys., 14, 5513–5527, 2014.
468 IPCC, 2013: Climate Change 2013: The Physical Science Basis. Contribution of Working Group I to
469 the Fifth Assessment Report of the Intergovernmental Panel on Climate Change, edited by:
470 Stocker, T. F., Qin, D., Plattner, G. K., Tignor, M., Allen, S. K., Boschung, J., Nauels, A., Xia, Y.,
471 Bex, V., and Midgley, P. M., Cambridge University Press, Cambridge, United Kingdom and New
472 York, NY, USA.
473 Kelly, E. N., Schindler, D. W., Hodson, P. V., Short, J. W., Radmanovich, R., and Nielsen, C. C.: Oil
474 sands development contributes elements toxic at low concentrations to the Athabasca River and
475 its tributaries, Proc. Natl. Acad. Sci. U.S.A., 107, 16178–16183, 2010.
476 Kelly, E. N., Short, J. W., Schindler, D. W., Hodson, P. V., Ma, M., Kwan, A. K., and Fortin, B. L.:
477 Oil sands development contributes polycyclic aromatic compounds to the Athabasca River and its
478 tributaries, Proc. Natl. Acad. Sci. U.S.A., 106, 22346–22351, 2009.

Kleinman, L. I., Springston, S. R., Daum, P. H., Lee, Y. N., Nunnermacker, L. J., Senum, G. I., Wang, J., Weinstein-Lloyd, J., Alexander, M. L., Hubbe, J., Ortega, J., Canagaratna, M. R., and Jayne, J.: The time evolution of aerosol composition over the Mexico City plateau, Atmos. Chem. Phys., 8, 1559–1575, 2008.

Kondo, Y., Matsui, H., Moteki, N., Sahu, L., Takegawa, N., Kajino, M., Zhao, Y., Cubison, M. J., Jimenez, J. L., Vay, S., Diskin, G. S., Anderson, B., Wisthaler, A., Mikoviny, T., Fuelberg, H. E., Blake, D. R., Huey, G., Weinheimer, A. J., Knapp, D. J., and Brune, W. H.: Emissions of black carbon, organic, and inorganic aerosols from biomass burning in North America and Asia in 2008, J. Geophys. Res., 116, D08204, doi:10.1029/2010JD015152, 2011a.

Kondo, Y., Sahu, L., Moteki, N., Khan, F., Takegawa, N., Liu, X., Koike, M., and Miyakawa, T.: Consistency and traceability of black carbon measurements made by laser-induced incandescence, thermal-optical transmittance, and filter-based photo-absorption techniques, Aerosol Sci. Technol., 45, 295–312, 2011b.

Kurek, J., Kirk, J. L., Muir, D. C. G., Wang, X., Evans, M. S., Smol, J. P.: Legacy of a half century of Athabasca oil sands development recorded by lake ecosystems, Proc. Natl. Acad. Sci. U.S.A., 110, 1761–1766, 2013.

Laborde, M., Crippa, M., Tritscher, T., Jurányi, Z., Decarlo, P. F., Temime-Roussel, B., Marchand, N., Eckhardt, S., Stohl, A., Baltensperger, U., Prévôt, A. S. H., Weingartner, E., and Gysel, M.: Black carbon physical properties and mixing state in the European megacity Paris, Atmos. Chem. Phys., 13, 5831–5856, 2013.

Laborde, M., Mertes, P., Zieger, P., Dommen, J., Baltensperger, U., and Gysel, M.: Sensitivity of the Single Particle Soot Photometer to different black carbon types, Atmos. Meas. Tech., 5, 1031–1043, 2012a.

Laborde, M., Schnaiter, M., Linke, C., Saathoff, H., Naumann, K. H., Möhler, O., Berlenz, S., Wagner, U., Taylor, J. W., Liu, D., Flynn, M., Allan, J. D., Coe, H., Heimerl, K., Dahlkötter, F., Weinzierl, B., Wollny, A. G., Zanatta, M., Cozic, J., Laj, P., Hitzenberger, R., Schwarz, J. P., and Gysel, M.:

505 Single Particle Soot Photometer intercomparison at the AIDA chamber, Atmos. Meas. Tech., 5,
506 3077–3097, 2012b.
507 Lambe, A. T., Cappa, C. D., Massoli, P., Onasch, T. B., Forestieri, S. D., Martin, A. T., Cummings, M.
508 J., Croasdale, D. R., Brune,W. H.,Worsnop, D. R., and Davidovits, P.: Relationship between
509 oxidation level and optical properties of secondary organic aerosol. Environ. Sci. Technol., 47,
510 6349–6357, 2013.
511 Langridge, J. M., Lack, D., Brock, C. A., Bahreini, R., Middlebrook, A. M., Neuman, J. A., Nowak, J.
512 B., Perring, A. E., Schwarz, J. P., Spackman, J. R., Holloway, J. S., Pollack, I. B., Ryerson, T. B.,
513 Roberts, J. M., Warneke, C., de Gouw, J. A., Trainer, M. K., and Murphy, D. M.: Evolution of
514 aerosol properties impacting visibility and direct climate forcing in an ammonia-rich urban
515 environment, J. Geophys. Res., 117, D00V11, doi:10.1029/2011JD017116, 2012.
516 Li, S. M., Leithead, A., Moussa, S. G., Liggio, J., Moran, M. D., Wang, D., Hayden, K., Darlington,
517 A., Gordon, M, Staebler, R., Makar, P. A., Stroud, C. A., McLaren, R., Liu, P., O'Brien, J.,
518 Mittermeier, R. L., Zhang, J., Marson, G., Cober, S. G., Wolde, M., and Wentzell, J.: Differences
519 between measured and reported volatile organic compound emissions from oil sands facilities in
520 Alberta, Canada, Proc. Natl. Acad. Sci. U.S.A., 114, E3756–E3765, 2017.
521 Liggio, J., Li, S. M., Hayden, K., Taha, Y. M., Stroud, C., Darlington, A., Drollette, B. D., Gordon, M.,
522 Lee, P., Liu, P., Leithead, A., Moussa, S. G., Wang, D., O'Brien, J., Mittermeier, R. L., Brook, J.
523 R., Lu, G., Staebler, R. M., Han, Y., Tokarek, T. W., Osthoff, H. D., Makar, P. A., Zhang, J.,
524 Plata, D. L., and Gentner, D. R.: Oil sands operations as a large source of secondary organic
525 aerosols, Nature, 534, 91–94, 2016.
526 Liggio, J., Moussa, S. G., Wentzell, J., Darlington, A., Liu, P., Leithead, A., Hayden, K., O'Brien, J.,
527 Mittermeier, R. L., Staebler, R., Wolde, M., and Li, S. M.: Understanding the primary emissions
528 and secondary formation of gaseous organic acids in the oil sands region of Alberta, Canada,
529 Atmos. Chem. Phys., 17, 8411-8427, 2017.
530 Liu, D., Allan, J. D., Young, D. E., Coe, H., Beddows, D., Fleming, Z. L., Flynn, M. J., Gallagher, M.
531 W., Harrison, R. M., Lee, J., Prevot, A. S. H., Taylor, J. W., Yin, J., Williams, P. I., and Zotter, P.:

Size distribution, mixing state and source apportionment of black carbon aerosol in London during wintertime, Atmos. Chem. Phys., 14, 10061–10084, 2014.

Liu, D., Flynn, M., Gysel, M., Targino, A., Crawford, I., Bower, K., Choularton, T., Jurányi, Z., Steinbacher, M., Hüglin, C., Curtius, J., Kampus, M., Petzold, A., Weingartner, E., Baltensperger, U., and Coe, H.: Single particle characterization of black carbon aerosols at a tropospheric alpine site in Switzerland, Atmos. Chem. Phys., 10, 7389–7407, 2010.

McMeeking, G. R., Hamburger, T., Liu, D., Flynn, M., Morgan, W. T., Northway, M., Highwood, E. J., Krejci, R., Allan, J. D., Minikin, A., and Coe, H.: Black carbon measurements in the boundary layer over western and northern Europe, Atmos. Chem. Phys., 10, 9393–9414, 2010.

Metcalf, A. R., Craven, J. S., Ensberg, J. J., Brioude, J., Angevine, W., Sorooshian, A., Duong, H. T., Jonsson, H. H., Flagan, R. C., and Seinfeld, J. H.: Black carbon aerosol over the Los Angeles Basin during CalNex, J. Geophys. Res., 117, D00V13, doi:10.1029/2011JD017255, 2012.

Morgenstern, O., Hegglin, M. I., Rozanov, E., O'Connor, F. M., Abraham, N. L., Akiyoshi, H., Archibald, A. T., Bekki, S., Butchart, N., Chipperfield, M. P., Deushi, M., Dhomse, S. S., Garcia, R. R., Hardiman, S. C., Horowitz, L. W., Jöckel, P., Josse, B., Kinnison, D., Lin, M., Mancini, E., Manyin, M. E., Marchand, M., Maréca, V., Michou, M., Oman, L. D., Pitari, G., Plummer, D. A., Revel, L. E., Saint-Martin, D., Schofield, R., Stenke, A., Stone, K., Sudo, K., Tanaka, T. Y., Tilmes, S., Yamashita, Y., Yoshida, K., and Zeng, G.: Review of the global models used within phase 1 of the Chemistry–Climate Model Initiative (CCMI), Geosci. Model Dev., 10, 639–671, 2017.

Moteki, N. and Kondo, Y.: Dependence of laser-induced incandescence on physical properties of black carbon aerosols: measurements and theoretical interpretation, Aerosol Sci. Technol., 44, 663–675, 2010.

Moteki, N., Kondo, Y., Miyazaki, Y., Takegawa, N., Komazaki, Y., Kurata, G., Shirai, T., Blake, D. R., Miyakawa, T., and Koike, M.: Evolution of mixing state of black carbon particles: aircraft measurements over the western Pacific in March 2004, Geophys. Res. Lett., 34, L11803, doi:10.1029/2006GL028943, 2007.

559 Moteki, N., Kondo, Y., and Nakamura, S.: Method to measure refractive indices of small nonspherical
560 particles: application to black carbon particles, J. Aerosol Sci., 41, 513–521, 2010.
561 Myhre, G., Samset, B. H., Schulz, M., Balkanski, Y., Bauer, S., Berntsen, T. K., Bian, H., Bellouin, N.,
562 Chin, M., Diehl, T., Easter, R. C., Feichter, J., Ghan, S. J., Hauglustaine, D., Iversen, T., Kinne,
563 S., Kirkevåg, A., Lamarque, J. F., Lin, G., Liu, X., Lund, M. T., Luo, G., Ma, X., van Noije, T.,
564 Penner, J. E., Rasch, P. J., Ruiz, A., Seland, Ø., Skeie, R. B., Stier, P., Takemura, T., Tsigaridis,
565 K., Wang, P., Wang, Z., Xu, L., Yu, H., Yu, F., Yoon, J. H., Zhang, K., Zhang, H., and Zhou, C.:
566 Radiative forcing of the direct aerosol effect from AeroCom Phase II simulations, Atmos. Chem.
567 Phys., 13, 1853–1877, 2013.
568 Parajulee, A. and Wania, F.: Evaluating officially reported polycyclic aromatic hydrocarbon emissions
569 in the Athabasca oil sands region with a multimedia fate model, Proc. Natl. Acad. Sci. U.S.A.,
570 111, 3344–3349, 2014.
571 Petzold, A., Ogren, J. A., Fiebig, M., Laj, P., Li, S. M., Baltensperger, U., Holzer-Popp, T., Kinne, S.,
572 Pappalardo, G., Sugimoto, N., Wehrli, C., Wiedensohler, A., and Zhang, X. Y.:
573 Recommendations for reporting “black carbon” measurements, Atmos. Chem. Phys., 13, 8365–
574 8379, 2013.
575 Ramanathan, V. and Carmichael G.: Global and regional climate changes due to black carbon, Nature
576 Geosci., 1, 221–227, 2008.
577 Sahu, L. K., Kondo, Y., Moteki, N., Takegawa, N., Zhao, Y., Cubison, M. J., Jimenez, J. L., Vay, S.,
578 Diskin, G. S., Wisthaler, A., Mikoviny, T., Huey, L. G., Weinheimer, A. J., and Knapp, D. J.:
579 Emission characteristics of black carbon in anthropogenic and biomass burning plumes over
580 California during ARCTAS-CARB 2008, J. Geophys. Res., 117, D16302,
581 doi:10.1029/2011JD017401, 2012.
582 Samset, B. H., Myhre, G., Herber, A., Kondo, Y., Li, S. M., Moteki, N., Koike, M., Oshima, N.,
583 Schwarz, J. P., Balkanski, Y., Bauer, S. E., Bellouin, N., Berntsen, T. K., Bian, H., Chin, M.,
584 Diehl, T., Easter, R. C., Ghan, S. J., Iversen, T., Kirkevåg, A., Lamarque, J. F., Lin, G., Liu, X.,
585 Penner, J. E., Schulz, M., Seland, Ø., Skeie, R. B., Stier, P., Takemura, T., Tsigaridis, K., and

586 Zhang, K.: Modelled black carbon radiative forcing and atmospheric lifetime in AeroCom Phase
587 II constrained by aircraft observations, Atmos. Chem. Phys., 14, 12465–12477, 2014.
588 Schnaiter, M., Linke, C., Möhler, O., Naumann, K. H., Saathoff, H., Wagner, R., Schurath, U.,
589 Wehner, B.: Absorption amplification of black carbon internally mixed with secondary organic
590 aerosol, J. Geophys. Res., 110, D19204. http://dx.doi.org/10.1029/2005JD006046, 2005.
591 Schwarz, J. P., Gao, R. S., Fahey, D. W., Thomson, D. S., Watts, L. A., Wilson, J. C., Reeves, J. M.,
592 Darbeheshti, M., Baumgardner, D. G., Kok, G. L., Chung, S. H., Schulz, M., Hendricks, J., Lauer,
593 A., Karcher, B., Slowik, J. G., Rosenlof, K. H., Thompson, T. L., Langford, A. O., Loewenstein,
594 M., and Aikin, K. C.: Single-particle measurements of midlatitude black carbon and light-
595 scattering aerosols from the boundary layer to the lower stratosphere, J. Geophys. Res., 111,
596 D16207, doi:10.1029/2006JD007076, 2006.
597 Schwarz, J. P., Gao, R. S., Spackman, J. R., Watts, L. A., Thomson, D. S., Fahey, D. W., Ryerson, T.
598 B., Peischl, J., Holloway, J. S., Trainer, M., Frost, G. J., Baynard, T., Lack, D. A., de Gouw, J. A.,
599 Warneke, C., and Del Negro, L. A.: Measurement of the mixing state, mass, and optical size of
600 individual black carbon particles in urban and biomass burning emissions, Geophys. Res. Lett.,
601 35, L13810, doi:10.1029/2008GL033968, 2008a.
602 Schwarz, J. P., Spackman, J. R., Fahey, D. W., Gao, R. S., Lohmann, U., Stier, P., Watts, L. A.,
603 Thomson, D. S., Lack, D. A., Pfister, L., Mahoney, M. J., Baumgardner, D., Wilson, J. C., and
604 Reeves, J. M.: Coatings and their enhancement of black carbon light absorption in the tropical
605 atmosphere, J. Geophys. Res., 113, D03203, doi:10.1029/2007JD009042, 2008b.
606 Schwarz, J. P., Spackman, J. R., Gao, R. S., Watts, L. A., Stier, P., Schulz, M., Davis, S. M., Wofsy, S.
607 C., and Fahey, D. W., Global-scale black carbon profiles observed in the remote atmosphere and
608 compared to models, Geophys. Res. Lett., 37, L18812, doi:10.1029/2010GL044372, 2010.
609 Shephard, M. W., McLinden, C. A., Cady-Pereira, K. E., Luo, M., Moussa, S. G., Leithead, A., Liggio,
610 J., Staebler, R. M., Akingunola, A., Makar, P., Lehr, P., Zhang, J., Henze, D. K., Millet, D. B.,
611 Bash, J. O., Zhu, L., Wells, K. C., Capps, S. L., Chaliyakunnel, S., Gordon, M., Hayden, K.,
612 Brook, J. R., Wolde, M., and Li, S. M.: Tropospheric Emission Spectrometer (TES) satellite

observations of ammonia, methanol, formic acid, and carbon monoxide over the Canadian oil sands: validation and model evaluation, Atmos. Meas. Tech., 8, 5189–5211, 2015.

Shiraiwa, M., Kondo, Y., Moteki, N., Takegawa, N., Miyazaki, Y., and Blake, D. R.: Evolution of mixing state of black carbon in polluted air from Tokyo, Geophys. Res. Lett., 34, L16803, doi:10.1029/2007GL029819, 2007.

Shiraiwa, M., Kondo, Y., Moteki, N., Takegawa, N., Sahu, L. K., Takami, A., Hatakeyama, S., Yonemura, S., and Blake, D. R.: Radiative impact of mixing state of black carbon aerosol in Asian outflow, J. Geophys. Res., 113, D24210, doi:10.1029/2008JD010546, 2008.

Stephens, M., Turner, N., and Sandberg, J.: Particle identification by laser-induced incandescence in a solid-state laser cavity, Appl. Opt., 42, 3726–3736, 2003.

Stier, P., Feichter, J., Kinne, S., Kloster, S., Vignati, E., Wilson, J., Ganzeveld, L., Tegen, I., Werner, M., Balkanski, Y., Schulz, M., Boucher, O., Minikin, A., and Petzold, A.: The aerosol-climate model ECHAM5-HAM, Atmos. Chem. Phys., 5, 1125–1156, 2005.

Taylor, J. W., Allan, J. D., Allen, G., Coe, H., Williams, P. I., Flynn, M. J., Le Breton, M., Muller, J. B. A., Percival, C. J., Oram, D., Forster, G., Lee, J. D., Rickard, A. R., Parrington, M., and Palmer, P. I.: Size-dependent wet removal of black carbon in Canadian biomass burning plumes, Atmos. Chem. Phys., 14, 13755–13771, 2014.

Taylor, J. W., Allan, J. D., Liu, D., Flynn, M., Weber, R., Zhang, X., Lefer, B. L., Grossberg, N., Flynn, J., and, Coe, H.: Assessment of the sensitivity of core/shell parameters derived using the single-particle soot photometer to density and refractive index, Atmos. Meas. Tech., 8, 1701–1718, 2015.

Atmos. Chem. Phys. Discuss., https://doi.org/10.5194/acp-2017-1015
Manuscript under review for journal Atmos. Chem. Phys.
Discussion started: 22 November 2017

Atmospheric Chemistry and Physics Discussions

Table 1. Variations of the parameters derived from time-resolved lognormal fits to single-particle rBC data measured during F_8/26 and F_8/28. Variations are determined as relative standard deviations (RSD, in %).

	MMD	$Width_{mass}$	$F_{rBC,\ mass}$	NMD	$Wdith_{number}$	$F_{rBC,\ number}$
F_8/26	1.46	4.42	2.82	4.48	5.30	4.07
F_8/28	6.85	8.46	9.47	7.94	7.18	8.07

Atmos. Chem. Phys. Discuss., https://doi.org/10.5194/acp-2017-1015
Manuscript under review for journal Atmos. Chem. Phys.
Discussion started: 22 November 2017

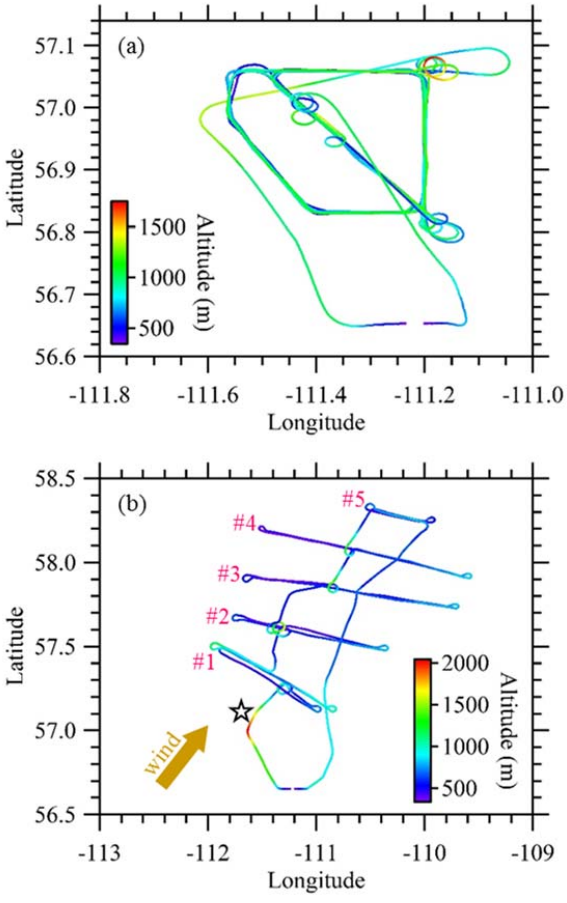

Figure 1. Examples of flight tracks for **(a)** emission and **(b)** transformation flights, which were flown on August 28 (F_8/28) and September 4 (F_9/4), 2013, respectively. F_8/28 was flown in a 5-sided polygon pattern, encircling the SUN facility. F_9/4 was conducted in a Lagrangian pattern, involving five virtual screens (#1 to #5) the first of which was located at the downwind edge of the OS source region. Distances between the successive flight screens during F_9/4 were approximately 30 km, whereas distance between the OS center (shown approximately by the open star) to screen#1 was also about 30 km. Refer to Liggio et al. (2016) for the Google Earth image that shows flight track of F_9/4 and locations of the multiple OS facilities. Altitude shown here indicates the ellipsoid height.

Atmos. Chem. Phys. Discuss., https://doi.org/10.5194/acp-2017-1015
Manuscript under review for journal Atmos. Chem. Phys.
Discussion started: 22 November 2017

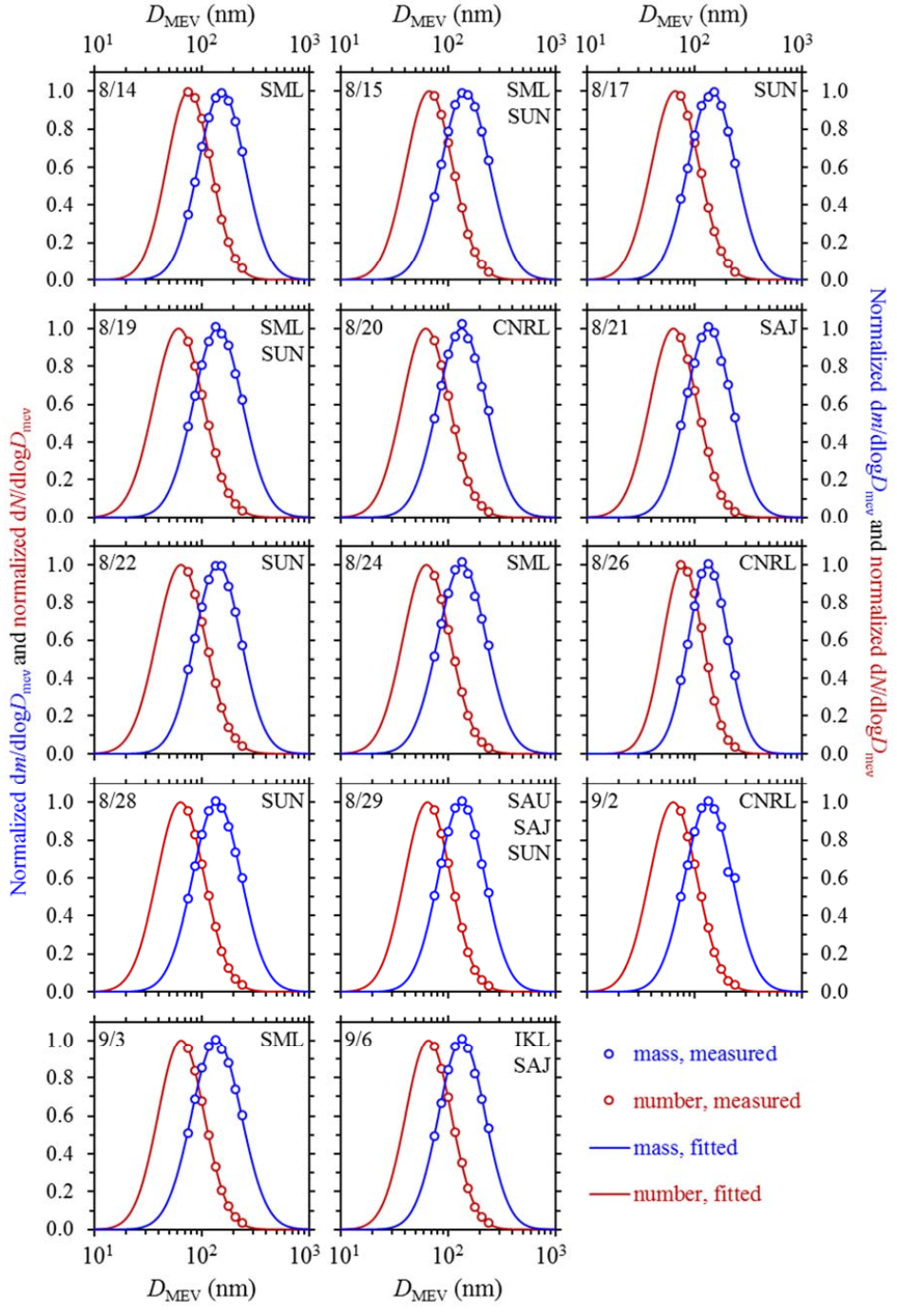

Figure 2. Mass and number size distributions of rBC for the 14 emission flights, which are derived from SP2 measurements over the OS facilities. Results from flight tracks between the airport and

Atmos. Chem. Phys. Discuss., https://doi.org/10.5194/acp-2017-1015
Manuscript under review for journal Atmos. Chem. Phys.
Discussion started: 22 November 2017

Atmospheric Chemistry and Physics Discussions

OS facilities are not involved in the analysis. Measurement date and the targeted OS facilities (1−3) are also shown for each flight. MMD, NMD, mass and number distribution widths, which are determined by lognormal fits to the measurement results, are summarized in Table S1 for these emission flights.

Atmos. Chem. Phys. Discuss., https://doi.org/10.5194/acp-2017-1015
Manuscript under review for journal Atmos. Chem. Phys.
Discussion started: 22 November 2017

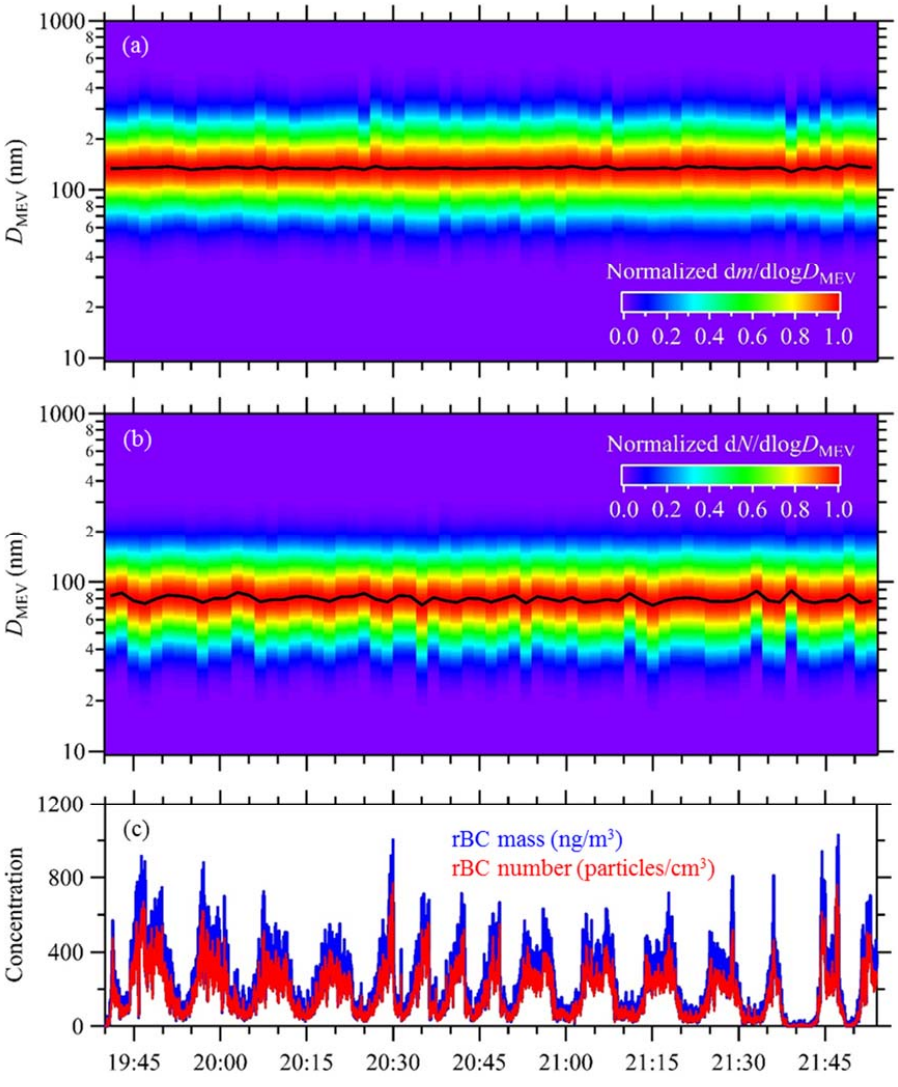

Figure 3. Time-resolved rBC **(a)** mass size distribution, **(b)** number size distribution, and **(c)** concentrations observed over the CNRL facility during F_8/26. Solid lines in (a) and (c) indicate MMD and NMD, respectively. The horizontal axis shows UTC time.

Atmos. Chem. Phys. Discuss., https://doi.org/10.5194/acp-2017-1015
Manuscript under review for journal Atmos. Chem. Phys.
Discussion started: 22 November 2017

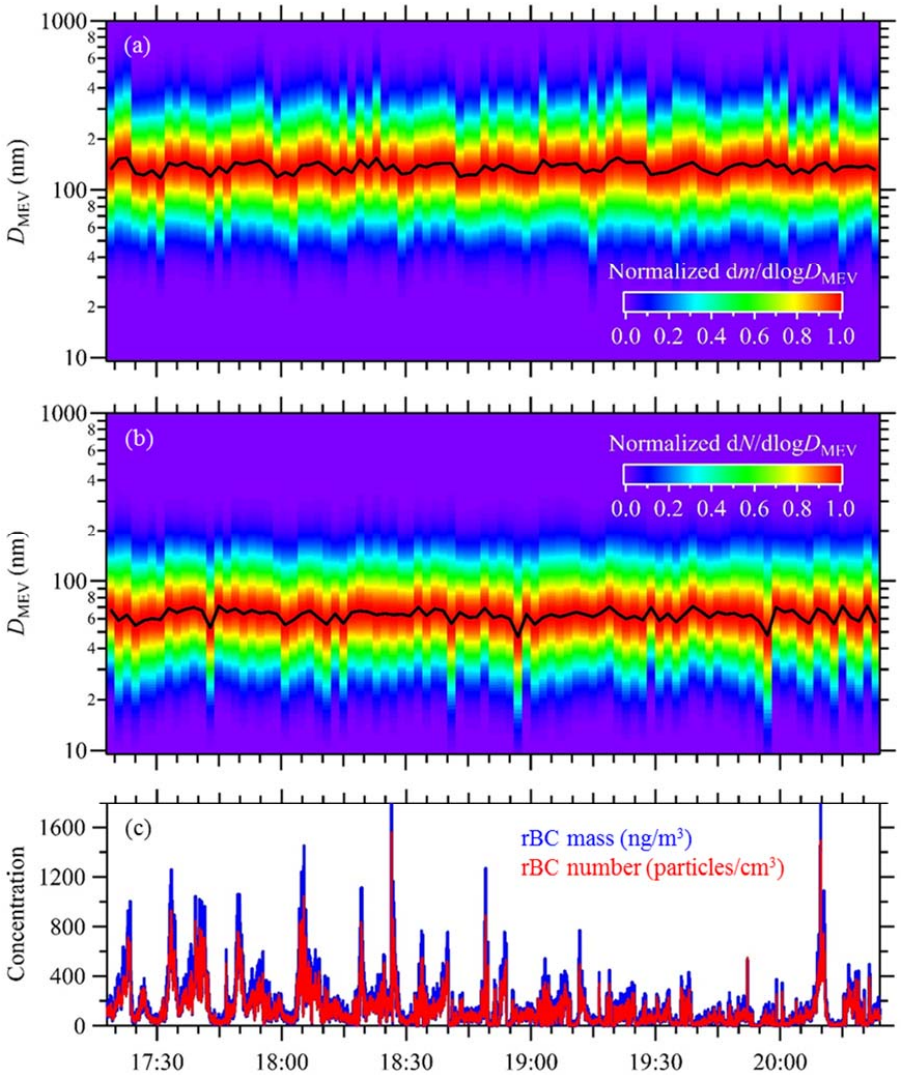

Figure 4. Time-resolved rBC **(a)** mass size distribution, **(b)** number size distribution, and **(c)** concentrations observed over the SUN facility during F_8/28. Solid lines in (a) and (c) indicate MMD and NMD, respectively. The horizontal axis shows UTC time. The flight track of F_8/28 is shown in Figure 1 (a).

Atmos. Chem. Phys. Discuss., https://doi.org/10.5194/acp-2017-1015
Manuscript under review for journal Atmos. Chem. Phys.
Discussion started: 22 November 2017

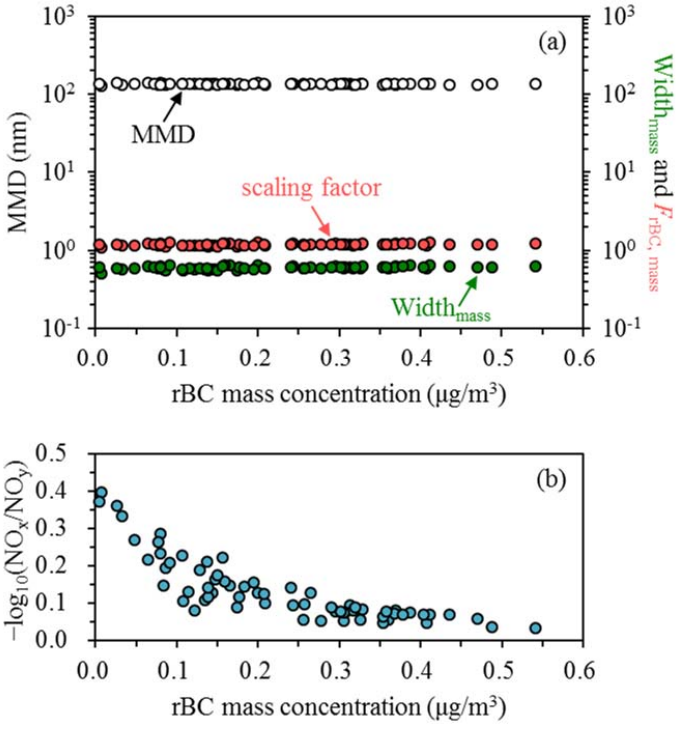

Figure 5. Dependences of **(a)** rBC MMD, mass distribution width (Width$_{mass}$), and mass-based scaling factor ($F_{rBC, mass}$), and **(b)** photochemical age on rBC concentration during F_8/26. Time resolution is 2 minutes for all the parameters shown here. Based on the temporal variation of 2-min averaged rBC mass concentration (Figure S1), rBC ≤ 0.1 μg/m^3 can be used as an indicator for typical out-of-plume conditions during F_8/26. Results in (a) are also available in Figure S1, where rBC MMD, Width$_{mass}$ and $F_{rBC, mass}$ are presented on linear scales.

Atmos. Chem. Phys. Discuss., https://doi.org/10.5194/acp-2017-1015
Manuscript under review for journal Atmos. Chem. Phys.
Discussion started: 22 November 2017

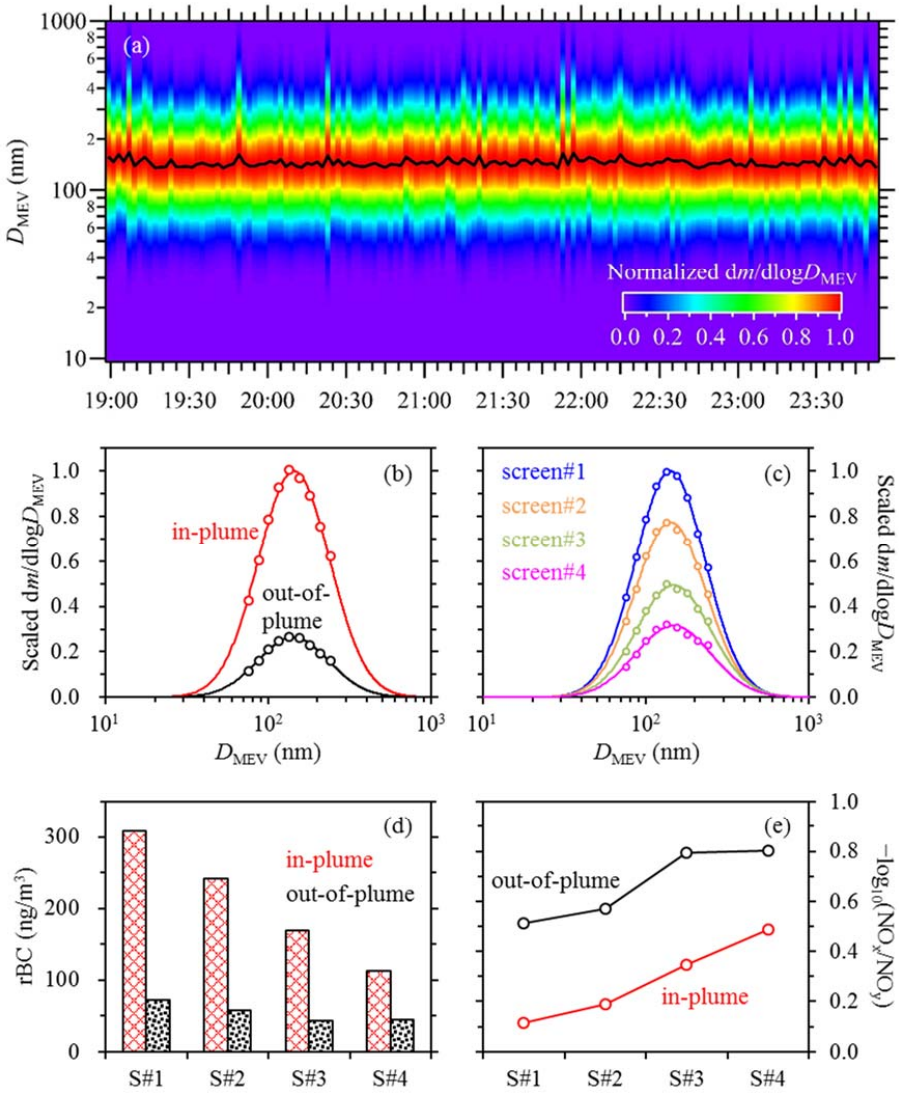

Figure 6. (a) Time-resolved rBC mass size distribution observed during the transformation flight F_9/4, **(b)** comparison of rBC mass size distribution between typical in- and out-of-plume conditions, **(c)** comparison of in-plume rBC mass size distribution among successive flight screens, and evolutions of **(d)** average rBC mass concentration and **(e)** photochemical age from screen #1 (S#1) to screen #4 (S#4). Scaling of out-of-plume rBC size distribution in (b), scaling of rBC size distributions for screens #2 to #4 in (c), and reason for excluding results from screen #5 in (c) to (e) are explained in the text.

Atmos. Chem. Phys. Discuss., https://doi.org/10.5194/acp-2017-1015
Manuscript under review for journal Atmos. Chem. Phys.
Discussion started: 22 November 2017

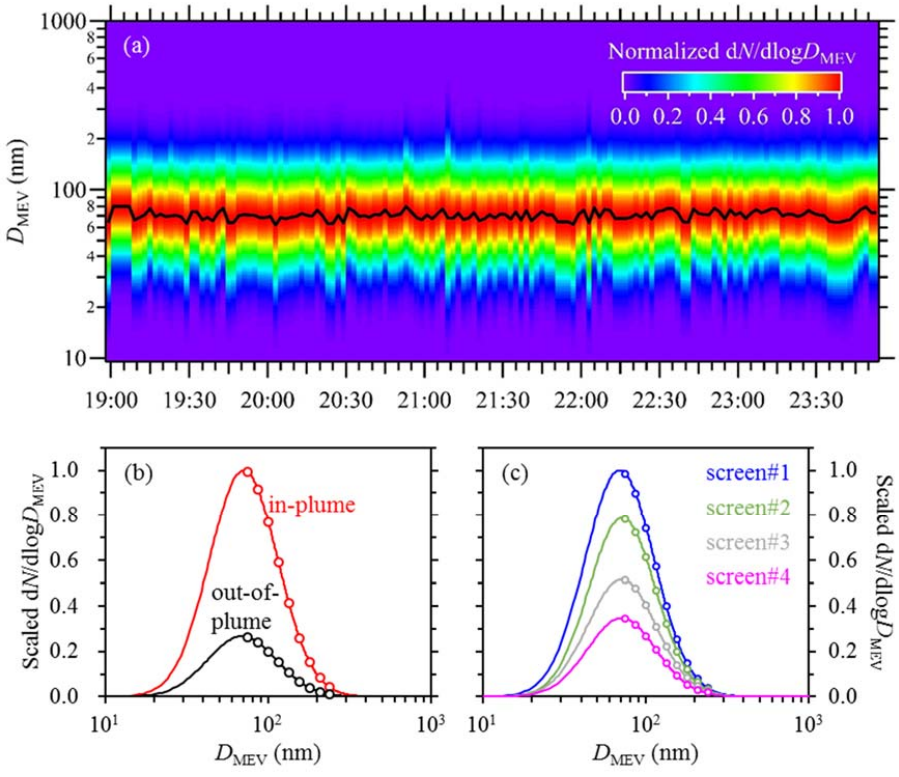

Figure 7. (a) Time-resolved rBC number size distribution observed during the transformation flight F_9/4, **(b)** comparison of rBC number size distribution between typical in- and out-of-plume conditions, and **(c)** comparison of in-plume rBC number size distribution among successive flight screens. Scaling of out-of-plume rBC size distribution in (b) and scaling of rBC size distributions for screens #2 to #4 in (c) are explained in the text.

Atmos. Chem. Phys. Discuss., https://doi.org/10.5194/acp-2017-1015
Manuscript under review for journal Atmos. Chem. Phys.
Discussion started: 22 November 2017

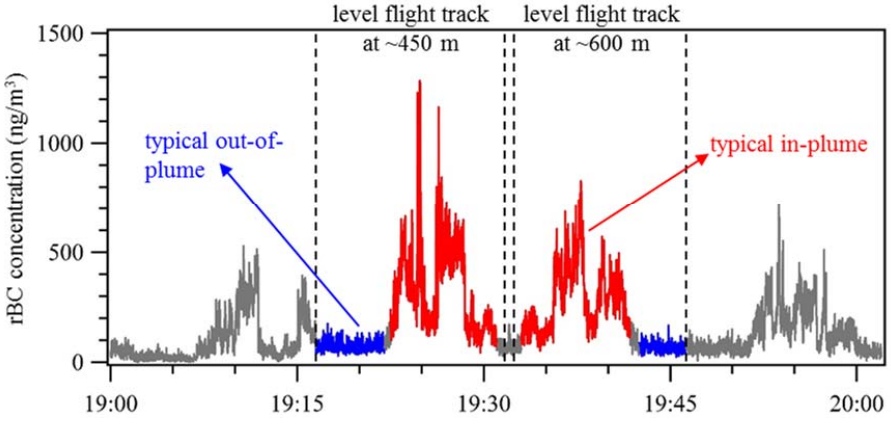

Figure 8. Identification of typical in- and out-of-plume conditions for two level flight tracks at ~ 450 and 600 m (in terms of ellipsoid height, equivalent to ~150 and 300 m above ground) on the first virtual screen of the transformation flight F_9/4.

Atmos. Chem. Phys. Discuss., https://doi.org/10.5194/acp-2017-1015
Manuscript under review for journal Atmos. Chem. Phys.
Discussion started: 22 November 2017

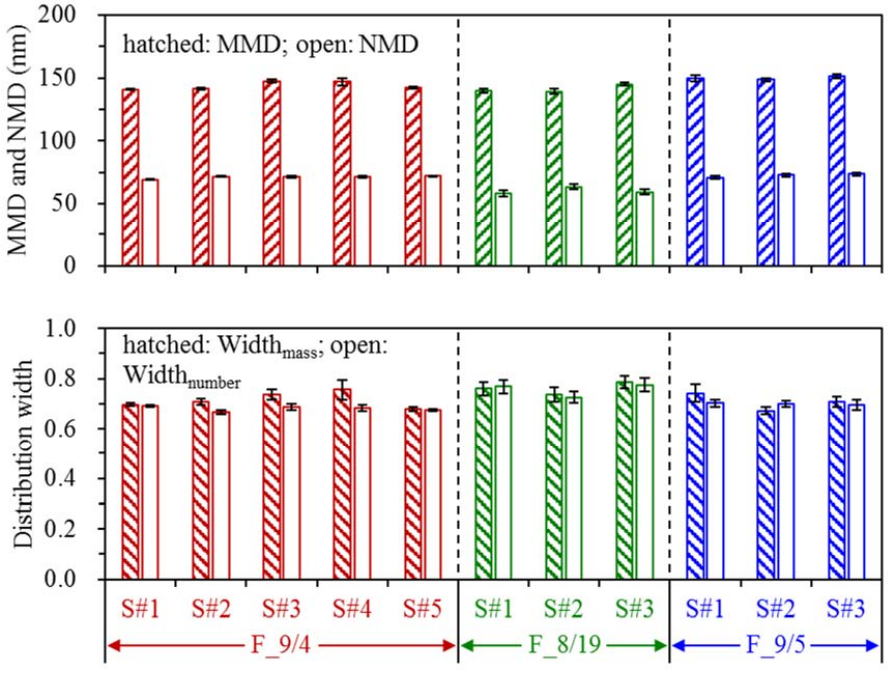

Figure 9. In-plume rBC MMD and NMD (upper pannel), and mass and number distribution widths ($Width_{mass}$ and $Width_{number}$; lower panel) derived from successive flight screens of the three transformation flights. The results are also available in Table S2.

Atmos. Chem. Phys. Discuss., https://doi.org/10.5194/acp-2017-1015
Manuscript under review for journal Atmos. Chem. Phys.
Discussion started: 22 November 2017

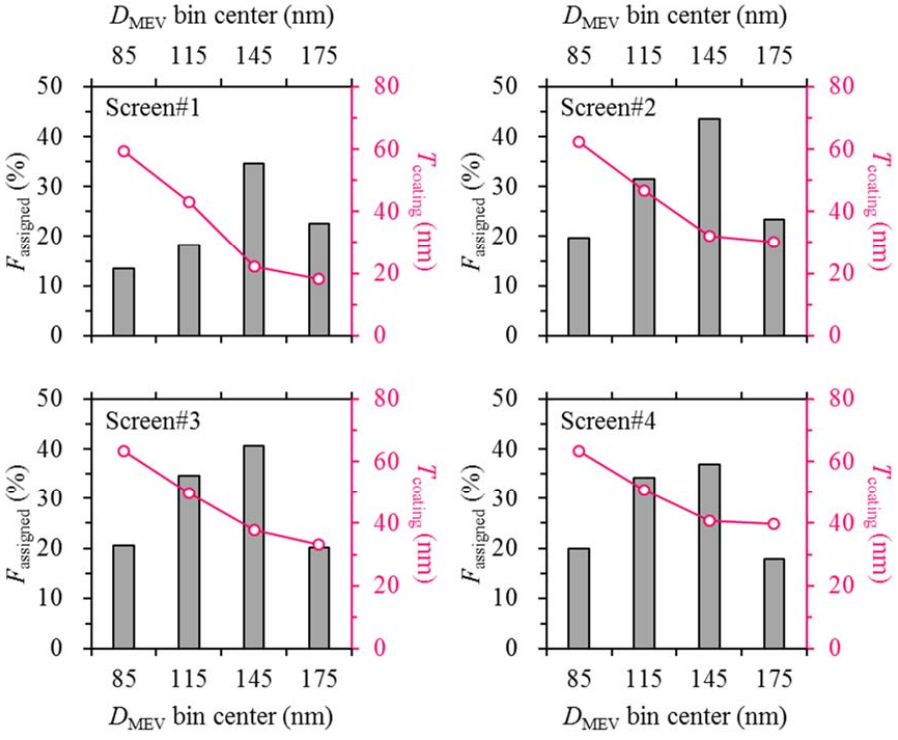

Figure 10. Dependence of coating thickness ($T_{coating}$) on rBC core size (D_{MEV}) for successive flight screens of the transformation flight F_9/4. To derive the dependence, rBC containing particles detected by the SP2 are divided into four equal-width bins according to their core sizes (D_{MEV}), the centers of which are 85, 115, 145, and 175 nm, respectively. The lower edge of the first D_{MEV} bin is 70 nm, corresponding to the SP2's lower detection limit of D_{MEV}; the upper edge of the last D_{MEV} bin is 190 nm. The D_{MEV} range of 70 to 190 nm accounts for approximately 95% of the detected rBC cores. For each D_{MEV} bin, the fraction of rBC cores that can be assigned a coating thickness ($F_{assigned}$, in %) is also shown.

Atmos. Chem. Phys. Discuss., https://doi.org/10.5194/acp-2017-1015
Manuscript under review for journal Atmos. Chem. Phys.
Discussion started: 22 November 2017

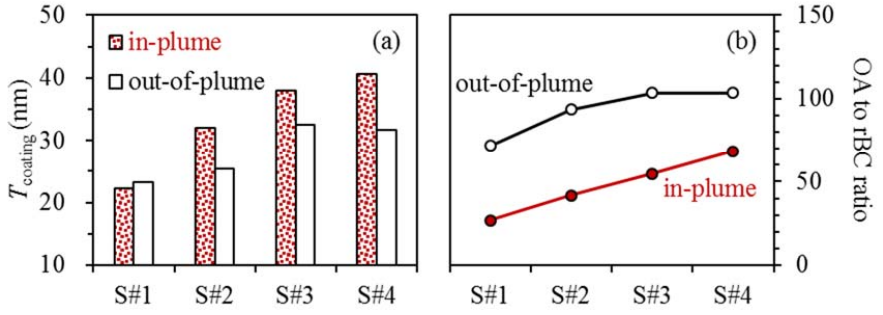

Figure 11. Evolutions of **(a)** coating thickness ($T_{coating}$) for rBC cores in the D_{MEV} range of 130−160 nm and **(b)** OA to rBC ratio (OA/rBC) during the transformation flight F_9/4. Only medians are shown for $T_{coating}$ and OA/rBC. Quantitative discussions on OA/rBC have been presented elsewhere (Liggio et al., 2016), whereas statistical results are shown in Figure S3 for $T_{coating}$ measured in F_9/4 (together with $T_{coating}$ measured in the other two transformation flights).

Atmos. Chem. Phys. Discuss., https://doi.org/10.5194/acp-2017-1015
Manuscript under review for journal Atmos. Chem. Phys.
Discussion started: 22 November 2017

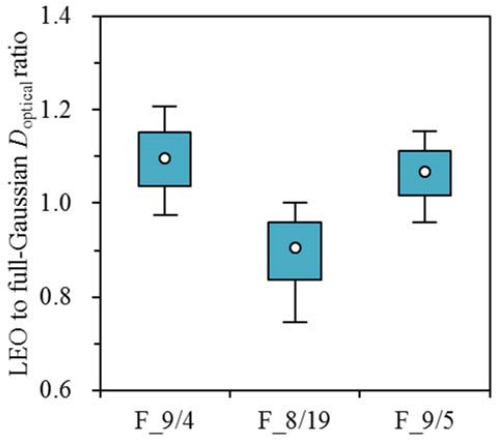

Figure 12. Relationships between optical sizes ($D_{optical}$) retrieved from the LEO and full-Gaussian fits for non-rBC containing particles observed during the three transformation flights.